

---

---

# Laser Vibration Sensing

Alan L. Kachelmyer and Kenneth I. Schultz

■ Laser vibration sensing has traditionally relied on limiters and frequency-modulation (FM) discriminators to process frequency-modulated laser radar returns. The performance of the traditional FM-discriminator approach can be limited by laser signature characteristics; both the temporal coherence of the laser and target speckle can degrade the performance of an FM-discriminator-based laser vibration sensor. We investigate a spectrogram-based frequency-demodulation technique that outperforms the traditional FM discriminator in the presence of both target speckle and limited laser temporal coherence. We compare the spectrogram and FM-discriminator techniques and present both theoretical and computer-simulation results for a vibrating diffuse or glint target with simple or complex piston motion that gives rise to FM-modulated return signals with speckle fading. Processed laser radar measurement data are used to add credibility to the results. These data include vibration signatures of the Low-Power Atmospheric Compensation Experiment (LACE) satellite.

**A**LASER VIBRATION SENSOR (LVS) can provide a noncontact means to measure minute vibrations of objects. The LVS is sensitive to vibration amplitudes that are on the order of the laser wavelength, or, in other words, sensitive to object skin displacements that are in the micrometer to millimeter regime. The LVS can be used for quality control in industrial applications in which vibration modes can identify product faults and machine malfunction. Solid state diode lasers offer the potential for a compact, inexpensive LVS, but their relatively poor coherence properties degrade the performance of the traditional signal processing method. In addition, because the laser wavelength is small compared to the height of the surface variations of the vibrating object, the reflected laser energy is diffused. This diffusion results in the so-called *speckle fading*, which occurs when there is motion of the laser beam over the surface of the object during the coherent measurement interval. The combination of speckle fading and laser phase noise due to poor coherence tends to reduce the performance of the traditional FM-discriminator method for processing the LVS vibration data.

The signal processing used to estimate target vibration depends on the properties of the measured signature. In particular, target vibration information is en-

coded in both the amplitude and phase of the reflected laser signal. The phase information imparts a frequency modulation onto the reflected waveform, requiring FM demodulation techniques to extract the vibration information. In this case, the vibration-induced time-varying amplitude fluctuations (i.e., the time-varying speckle pattern) manifests itself as noise in conventional FM demodulation techniques, which can result in significant degradation in FM demodulation performance. These time-varying amplitude fluctuations, however, do carry target vibration information that can be estimated by using appropriate signal processing techniques [1, 2, 3]. While the spectrogram technique can process both the amplitude and phase information, the analysis we present in this article is primarily concerned with processing the phase-encoded vibration signature.

A processing technique based on a spectrogram approach has proven to be more robust than conventional FM-discriminator-based techniques in the presence of laser speckle and/or laser phase noise. The spectrogram technique is more robust because of its ability to operate (1) at a lower carrier-to-noise ratio (CNR), (2) in the presence of fast speckle fading, (3) with a modest short-term laser coherence requirement, and (4) in spite of the phase noise of the local-

oscillator (LO) laser. This operational ability relaxes the stability requirements of the measurement platform and leads to more robust laser vibrometers that can operate in a difficult environment. In this article, theoretical results are presented in the high-CNR regime; these results show a 6-dB advantage for speckle targets processed with the spectrogram rather than the FM-discriminator method. The speckle-target case produces statistics that are equivalent to those of a Rayleigh-fading FM communications channel. For instance, with a 6-dB advantage, the range of an FM station in the presence of fading would be doubled with a spectrogram receiver.

We do not obtain generalized theoretical results for the spectrogram processor because of the difficulty of analyzing the FM-discriminator performance at low CNR. We do continue the comparison of the two processing methods, however, through the use of modeling and computer simulation. We model the vibrating diffuse target by assuming it behaves according to either a simple or a complex piston motion, or vibration, that gives rise to an FM-modulated return signal with speckle fading. The noise statistics of the FM-discriminator process with a diffuse target are completely different from those of the traditional glint (no speckle fading) target case, in which the output noise-power density is proportional to the output frequency squared.

We first model the high-CNR single-tone no-phase noise case for both the glint-target and diffuse-target examples, and compare it with the theoretical results. Next we model a two-tone complex vibration, and then we simulate other cases, including low CNR and LO phase noise, and give performance comparisons of the two processes. Finally, we use the spectrogram technique to obtain measured vibration signatures from the Low-Power Atmospheric Compensation Experiment (LACE) satellite.

### Continuous-Wave Spectrogram Processing

In the continuous-wave (CW) spectrogram approach, a laser vibrometer continuously transmits a CW laser signal that is directed at the target of interest. A passive angular acquisition-and-tracking system keeps the laser beam at approximately the same spot on the target over the measurement interval. If the vibration-

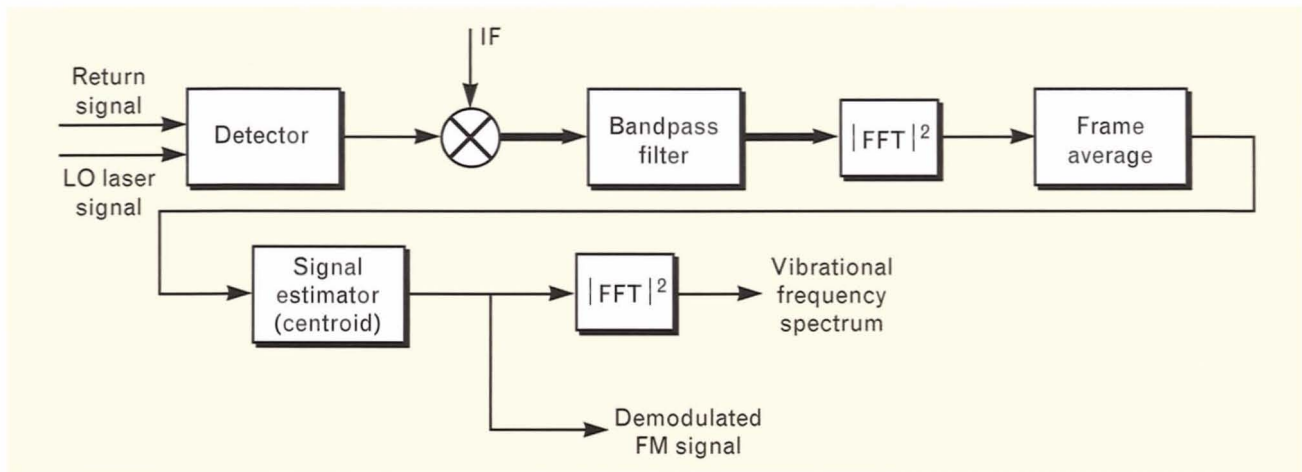
al modes are spatially invariant, then the angular tracking and pointing requirements are minimal. That is, the laser beam merely has to stay on the target of interest during the measurement interval. If, however, the target is moving with respect to the laser vibrometer, the velocity-induced Doppler shift must be tracked to process the residual vibration-induced signature.

Figure 1 shows a block diagram of the spectrogram processor. The FM-modulated return signal is offset-homodyne detected by optically mixing with the LO laser. The difference frequency signal out of the detector contains the translational Doppler frequency  $f_D$ , which is removed by the first in-phase and quadrature mixing stage. The mixer output is low-pass filtered and then sampled at an A/D conversion rate consistent with the expected bandwidth of the FM-modulated return.  $N$  complex samples are collected over the process coherence time  $T_c$  to form the first record, or *sample set*, which is then input into a Fast Fourier Transform (FFT). The envelope squared of the FFT output from the first record is then buffered. The next record is processed in similar fashion until  $q$  such FFT outputs are gathered and then averaged.

The  $N$  frequency bins from the averaged  $q$  consecutive records are then input to a centroid algorithm that estimates the frequency of the FM-modulated input signal. The frequency estimate is buffered and the entire process is repeated until the end of the measurement interval  $T_m$  is reached. The frequency estimates of number  $N_T = T_m/(qT_c)$  are then input into a final FFT processor that outputs the vibrational frequency spectrum.

### Range-Resolved Spectrogram Processor

The concept of laser vibrometry can be extended to include a range-resolved vibration spectrum. This concept eliminates potential background clutter from objects in front of or behind the target when the laser beam intercepts an area larger than the target area. The range-resolved laser vibrometer continuously transmits a laser beam whose optical carrier is frequency modulated by a train of linear-frequency-modulated (LFM) chirp pulses directed at the target of interest. Again, a passive angular acquisition-and-tracking system is required to keep the laser beam at



**FIGURE 1.** Block diagram of the continuous-wave (CW) spectrogram processor. The detected FM signal is mixed to an intermediate frequency, bandpass filtered, and Fourier transformed over a short time interval to track its instantaneous frequency and, hence, perform demodulation. Frame averaging of the short-time spectral outputs can be performed to reduce the speckle noise fluctuations before the frequency estimate is made.

approximately the same spot on the target over the measurement interval.

Figure 2 shows a block diagram of the range-resolved spectrogram processor. This processor is a multichannel variation of the CW spectrogram processor of Figure 1, in which spectrogram processing is performed at each of the range-resolved channels. The return LFM chirp-pulse-train waveform, which is also FM modulated by the target vibrations, is offset-homodyne detected by optically mixing with the LO laser. The difference frequency signal out of the detector contains the translational Doppler frequency  $f_D$  as well as the LFM chirp and target FM modulation. The Doppler frequency is removed by the first mixing stage whose output is centered at the desired IF frequency of the pair of surface acoustic wave (SAW) matched filters that perform the LFM chirp-pulse compression.

The complex compression filter output from both the in-phase and quadrature channels is sampled at an A/D conversion rate that is consistent with the LFM chirp-pulse bandwidth, which is usually much greater than the expected bandwidth of the FM-modulated return.  $N$  complex samples are collected over each chirp-pulse duration to provide for  $N$  range bins, or *range channels*. In each range channel,  $M$  complex samples, corresponding to the number of chirp pulses over the process coherence time  $T_c$ , form the first

record, or sample set, which is then input into an FFT.

In each range channel, the envelope squared of the FFT output from the first record is buffered. The next record is processed in similar fashion until  $q$  such FFT outputs are gathered and then averaged. In each range channel, the  $M$  averaged frequency bins, from the  $q$  consecutive records, are input to a centroid algorithm that estimates the frequency of the FM-modulated input signal. Each frequency estimate is buffered and the entire process is repeated until the end of the measurement interval  $T_m$  is reached. Finally, the frequency estimates of number  $N_T = T_m/(qT_c)$  are then input into a final FFT processor that outputs the vibrational frequency spectrum at that particular range bin.

#### *Spectrogram Signal-to-Noise-Ratio Analysis*

The CW spectrogram process shown in Figure 1 and the range-resolved spectrogram process shown in Figure 2 are based on estimating target vibration frequencies from the time evolution of a sequence of Doppler spectra. The spectrogram processing steps are given in Table 1.

We assume an input carrier-to-noise ratio  $CNR_{in}$  measured over the input bandwidth  $B_{in}$ , with a constant background-noise power spectral density, and we compute the CNR in the intermediate frequency (IF) bandwidth subsequent to the initial Fourier

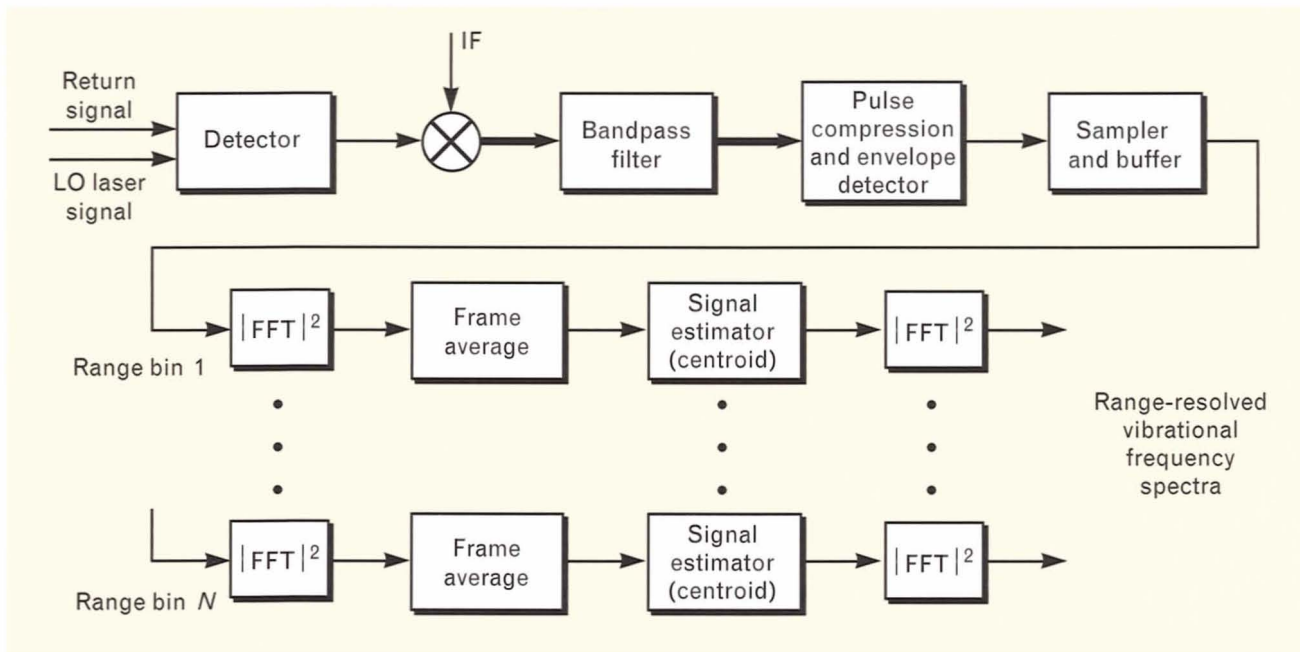


**FIGURE 2.** Block diagram of the range-resolved spectrogram processor. This processor is a multichannel version of the processor in Figure 1. Spectrogram processing is performed at each of the channels, and each channel corresponds to a different range.

transform. The CNR associated with the IF bandwidth  $B_{IF}$  is given by the following expression:

$$\text{CNR} = \frac{B_m}{\max(B_s, B_{IF})} \text{CNR}_{in},$$

where  $B_s$  is the speckle bandwidth. (If, of course, the noise bandwidth  $B_n$  is smaller than the IF bandwidth  $B_{IF}$ , then  $B_{IF}$  is replaced with  $B_n$ . In an LO shot-noise-limited LVS, the noise bandwidth and IF bandwidth are equal.) Intuitively, we see that the CNR improves with decreasing IF bandwidth, at least until the speckle bandwidth of the signal is equal to the IF bandwidth. If the IF bandwidth is made smaller than the speckle bandwidth, then the CNR is not improved because both the signal and noise are removed by the IF filter.

Let us assume that the target is diffuse and that the receiver is LO shot-noise limited. Because the target is diffuse, the in-phase and quadrature components of the IF signal-plus-noise complex envelope have Gaussian distributions. Each frequency bin of the Fourier-transformed IF signal, or *IF spectrum*, is a complex sample whose in-phase and quadrature components

also have Gaussian distributions. Each magnitude-squared complex frequency-bin sample is Rayleigh distributed with a signal mean given by CNR and a noise mean and variance of unity, by definition.

We now estimate the variance, or *noise power*, associated with the center-of-mass centroid calculation. To simplify the analysis, we employ the following assumptions: (1) the centroid tracking window encompasses the signal, or IF spectrum; (2) the signal and background noise have uniform average values; (3) the receiver is operating in the LO shot-noise-limited regime; (4) spectral frequency bins, or pixels, are uncorrelated; (5) the number of signal-plus-noise pixels is large; and (6) the signal is approximately centered in the tracking window (i.e., the signal has been acquired and is being tracked in frequency).

The variance of the centroid estimate of a  $q$ -frame-averaged IF spectrum (after the first short-time FFT) can be shown to be of the form

$$\sigma_c^2 = \frac{B_c(B_s^2 - B_c^2)}{12qB_s}. \quad (1)$$

where  $B_c = 1/T_c$  is the coherence time bandwidth. (See

**Table 1. Spectrogram Processing Steps**

1. Perform coherent infrared frequency offset-homodyne detection.
2. Perform translational Doppler frequency track to mix signal down to constant IF.
3. Filter signal to bandwidth  $B_{IF}$ .
4. Repeat the following steps over the entire measurement interval of length  $T_m$ .
  - a. Sample the filtered IF signal over coherent interval of length  $T_c$ .
  - b. Fourier-transform samples to obtain IF spectrum with bandwidth  $B_{IF}$ .
  - c. Frame-average spectra from consecutive intervals of length  $T_c$  to reduce speckle effects and reduce the centroid variance.
  - d. Estimate the frequency centroid of the frame-averaged IF spectrum.
5. Fourier-transform the centroid-estimates-versus-time data to obtain vibration spectrum.

the appendix at the end of the article for a detailed calculation of the variance of the centroid estimate.) We relate the centroid jitter variance to the background noise level in the vibration spectrum in the following manner. The  $q$ -frame-averaged centroid samples have an associated bandwidth of  $1/(qT_c)$ , where  $qT_c$  is the time interval between samples. Thus the power spectral density at the output of the final FFT, associated with the centroid jitter, is simply  $q\sigma_c^2/B_c$ . By using Equation 1, we determine the resultant expression for the noise power within the spectral bandwidth  $B_r$  for the  $q$ -frame-averaged centroid estimates to be

$$\sigma_n^2 = q\sigma_c^2 B_r / B_c = \frac{B_r(B_s^2 - B_c^2)}{12B_s}. \quad (2)$$

Notice that the noise power does not depend on the number  $q$  of spectral, or frame, averages. By assuming a modulation index and vibration frequency equal to  $\beta$  and  $f_m$ , respectively, we can express the signal power  $P_S$  for a single FM tone as

$$P_S = \frac{(\beta f_m)^2}{4}. \quad (3)$$

By using Equation 2 and Equation 3, we can express the spectrogram processor's output signal-to-noise

ratio  $\text{SNR}_{out}$  by

$$\text{SNR}_{out} = \frac{P_S}{\sigma_n^2} = \frac{3\beta^2 f_m^2 B_s}{B_r(B_s^2 - B_c^2)}. \quad (4)$$

If the speckle bandwidth  $B_s$  is much greater than the bin-size bandwidth  $B_c$ , then the output SNR is approximated by

$$\text{SNR}_{out} \approx \frac{3\beta^2 f_m^2}{B_r B_s}. \quad (5)$$

As we show in the following section, this approximate spectrogram output SNR is four times better than the corresponding output SNR obtained for the conventional FM discriminator.

#### *Glint-Target Case*

In the glint-target case we assume that the desired signal frequency is within the central bin of the centroid algorithm, and for simplicity we assume that an equal number ( $M/2$ ) of noise-only frequency bins of size  $B_c$  exist on either side of the desired signal frequency. Let  $M$  be the number of noise-only bins such that  $M = B_n/B_c$  with the noise bandwidth given by  $B_n$ . By modifying the analysis in the previous section, we find that the variance of the center-of-mass centroid algorithm becomes

$$\sigma_c^2 = \frac{2B_c^2 S_{M/2}}{(M+1 + \sqrt{B_n/B_c} \text{CNR})^2},$$

in which the mean noise intensity for each noise-only sample is unity and the mean signal intensity is just the CNR, and the CNR is measured with respect to the noise bandwidth  $B_n$ . The variance of the noise samples out of the first FFT is reduced by the coherent factor, or reduced-noise-bandwidth factor, of  $B_n/B_c$ . The summation  $S_{M/2}$  is given by

$$S_{M/2} = \frac{(M+2)(M+1)M}{24}.$$

The noise variance of the frequency samples in the final FFT is just

$$\sigma_n^2 = \frac{B_r \sigma_c^2}{B_c}.$$

The output SNR for the spectrogram-processed glint target becomes

$$\begin{aligned} \text{SNR}_{out} &= \frac{P_s}{\sigma_n^2} \\ &= \frac{3\beta^2 f_m^2 (B_n/B_c + 1 + \sqrt{B_n/B_c} \text{CNR})^2}{B_r B_n (B_n/B_c + 1)(B_n/B_c + 2)} \\ &\approx \frac{3\beta^2 f_m^2 B_c \text{CNR}^2}{B_r B_n^2}, \end{aligned} \quad (6)$$

where by definition  $B_n > B_c$ . The approximation is valid when the number of noise-only bins is large ( $B_n/B_c \gg 2$ ) and, simultaneously, when the CNR is high ( $\text{CNR} \gg \sqrt{B_n/B_c}$ ).

When the CNR is high and the value of  $B_n/B_c$  is small, or when the noise bandwidth is much smaller than the IF bandwidth, the simulation performance (which more closely represents actual system performance) is considerably better than the theoretical expression shown in Equation 6 indicates. This difference in performance occurs because the weight of the high-CNR signal sidebands in the high-frequency bins without noise reduces the centroid variance. The contribution of the signal sidebands to the output SNR was not included in the theoretical expression.

### FM Discriminator SNR Analysis

For completeness, laser phase noise is included in the following analysis of the FM-discriminator performance. Laser phase noise is not included, however, in the analytic performance comparisons of the two processors. Some simulation results that do include laser phase noise will be given later.

Figure 3 shows a block diagram of the conventional FM discriminator. In the digital version of the FM discriminator the derivative operation is performed by a two-point differencing of the consecutive samples. An ideal limiter operation is performed by computing the magnitude and phase (polar form) of each complex-envelope sample and then creating a new ideally limited complex-envelope sample by setting the magnitude equal to unity (or a constant value) and keeping the actual phase angle. If the measurement receiver does not supply complex samples—that is, it does not contain both an in-phase and quadrature channel—then the single-channel real data are first Hilbert transformed to create the complex envelope of the IF signal, which then allows for ideal limiting.

The return signal from a diffuse target illuminated by a continuously transmitted CW signal of radian carrier frequency  $\omega_0$  is given by

$$\begin{aligned} r(t) &= \text{Re}\{A_s(t) \exp[j\Phi_s(t)] \\ &\quad \times \exp[j\omega_0(t - d(t)) + j\Phi(t - d(t))]\}, \end{aligned}$$

where  $d(t)$  is the time-varying delay due to the round-trip path variation,  $A_s(t)$  and  $\Phi_s(t)$  are the speckle-induced amplitude and phase variation of the complex signal envelope, and  $\Phi(t)$  is the laser phase noise of the transmitted signal. We assume a homodyne system with an LO signal of the form

$$S_{LO}(t) = \text{Re}\{\exp[j(\omega_0 t + \Phi(t))]\}.$$

The IF detector output is of the form

$$\begin{aligned} r_0(t) &= \text{Re}\{A_s(t) \exp[j(\omega_0 d(t) - \Phi_s(t) + \Phi_p(t))]\} \\ &\quad + n_{LO}(t), \end{aligned}$$

where  $\Phi_p(t) = \Phi(t) - \Phi(t - d(t))$  is the laser phase-noise difference signal between the LO signal

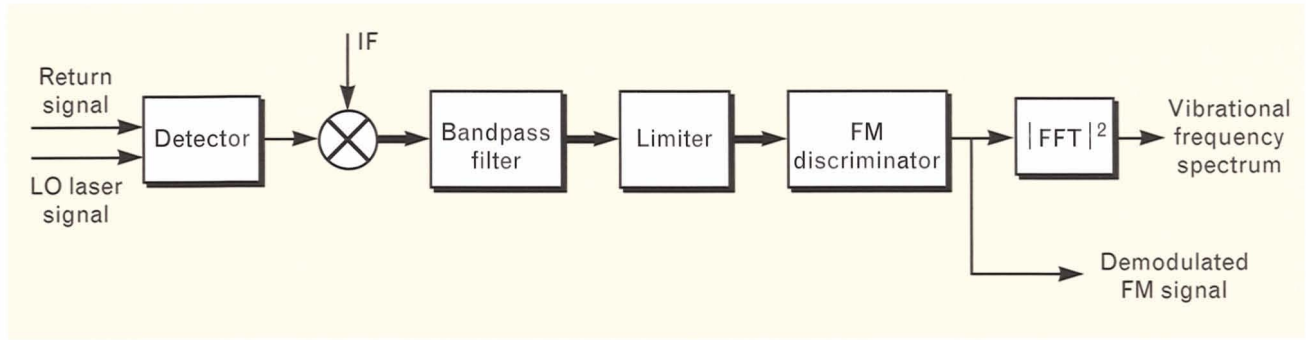


**FIGURE 3.** Conventional FM-discriminator process. This processor first performs a hard limiting of the signal to remove amplitude fluctuation and then performs a differentiation operation (via the FM-discriminator block) to recover the modulating signal.

and the delayed return signal, and where  $n_{LO}(t)$  is the LO shot noise. The time delay  $d(t)$  is of the form

$$d(t) = \frac{2R(t)}{c} = \frac{2}{c}[R_0 + vt + S(t)],$$

where  $v$  is the relative translational velocity of the target,  $R_0$  is the initial range, and  $S(t)$  represents the simple piston motion of the target skin. If we assume perfect Doppler-frequency compensation (after the first mixing stage), then the IF signal is of the form

$$\begin{aligned} r_0(t) &= \text{Re}\{A(t) \exp[j\Psi(t)]\} \\ &= \text{Re}\{A_s(t) \exp[j\Omega(t)]\} + n_{LO}(t), \end{aligned}$$

where

$$\Omega(t) = \frac{4\pi S(t)}{\lambda} - \Phi_s(t) + \Phi_p(t) + 2\pi f_{IF}t,$$

and where  $f_{IF}$  is the desired intermediate frequency after mixing. For simple piston motion the signal variation is of the form

$$\frac{4\pi S(t)}{\lambda} = \beta \sin \omega_m t,$$

with modulation index  $\beta$  and radian modulation frequency  $\omega_m$ .

In the high-CNR case (i.e., no shot noise), the ideally limited phase of the IF signal becomes

$$\Psi(t) = \Omega(t).$$

The FM-discriminator output is proportional to the time derivative of the phase; i.e.,

$$\dot{\Psi}(t) = \frac{4\pi \dot{S}(t)}{\lambda} - \dot{\Phi}_s(t) + \dot{\Phi}_p(t) + 2\pi f_{IF}.$$

The SNR of the discriminator output for simple piston motion becomes

$$\text{SNR}_{out} = \frac{(\beta\omega_m/2)^2}{N_s + N_p}, \quad (7)$$

where  $N_s$  and  $N_p$  are the noise powers due to the differentiated target-speckle noise and LO phase noise, respectively.

Let us assume that the target-speckle phase is correlated, with the autocorrelation function given by

$$R_{\Phi_s}(\tau) = \begin{cases} \sigma^2(1 - 2|\tau|/T) & -T/2 < \tau < T/2 \\ 0 & \text{otherwise} \end{cases}. \quad (8)$$

The speckle bandwidth is defined to be  $B_s = 1/T$  and the variance of the uniformly distributed phase samples is given by  $\sigma^2 = \pi^2/3$ . The autocorrelation function of the derivative of the phase is given by

$$R_{\dot{\Phi}_s}(\tau) = \frac{4\sigma^2}{T} \delta(\tau)$$

and the corresponding power spectral density function is

$$G_{\dot{\Phi}_s}(f) = \int_{-\infty}^{\infty} R_{\dot{\Phi}_s}(\tau) e^{-j2\pi f\tau} d\tau = \frac{4\sigma^2}{T}.$$

The speckle noise collected by a filter of bandwidth,

or resolution,  $B_r$  centered about the desired signal frequency  $f_m$  becomes

$$N_s = \frac{4\sigma^2 B_r}{T} = \frac{4B_r B_s \pi^2}{3}. \quad (9)$$

Consider now the laser phase noise of the homodyne-detected signal. Assume that the variations of the phase functions with respect to the minute time variations of the displacement  $d$  are insignificant over the measurement interval (i.e.,  $d(t) = d = \text{constant}$ ). The power spectral density of the difference phase function is easily shown to be

$$G_{\dot{\phi}_p}(f) = 4 \sin^2(\pi f d) G_{\dot{\phi}}(f).$$

If we again assume that the phase is uniformly distributed over  $2\pi$  radians, and that the correlation function is of the same form as in Equation 8 but with correlation time  $T_p$ , then the phase noise collected by a filter of bandwidth  $B_r$  centered about the desired signal frequency  $f_m$  becomes

$$N_p = \frac{[4 \sin^2(\pi f d)] 4 B_r B_p \pi^2}{3}, \quad (10)$$

where  $B_p = 1/T_p$  is the phase noise bandwidth. By using Equations 9 and 10, we see that the output SNR of an FM discriminator from Equation 7 in the no-shot-noise case becomes

$$\text{SNR}_{out} = \frac{3\beta^2 f_m^2}{4B_r[B_s + 4B_p \sin^2(\pi f d)]}. \quad (11)$$

D.N. Barr of the Night Vision and Electrooptics Laboratory in Fort Belvoir, Virginia, derived an approximate expression for the output SNR of a conventional FM discriminator for the case of a diffuse vibrating surface. The experimentally validated result, which is based on conventional FM click analysis, does not take into account laser phase noise and is valid for CNR values greater than 3 dB. The resultant expression is

$$\text{SNR}_{out} = \frac{\sqrt{3}\beta^2 f_m^2}{2B_r \left[ B_s + \frac{(B_{IF} - B_s)}{2 \text{CNR}} \right]}.$$

For high CNR the expression is approximated by

$$\text{SNR}_{out} \approx \frac{\sqrt{3}\beta^2 f_m^2}{2B_r B_s}. \quad (12)$$

The approximate spectrogram output SNR expression given by Equation 5 can be compared to the FM-discriminator output SNR expressions given by Equations 11 and 12. Thus, if we assume that the laser phase noise is negligible, the spectrogram process is theoretically 6 dB better than the conventional FM-discriminator process for the case of high CNR. The analysis by Barr shows the spectrogram process to be 5.4 dB better. An analytic estimate of the FM-discriminator performance for an arbitrary CNR is difficult to obtain, but a computer can easily simulate the exact performance for specific parameter sets.

#### *Glint-Target Case*

The complex envelope of the offset-homodyne-detected glint-target return IF signal is of the form

$$r_0(t) = A e^{j\beta \sin \omega_m t} + n(t),$$

where  $A$  is the carrier amplitude and  $n(t)$  is the complex Gaussian-distributed noise envelope. In the high-CNR regime we can show that the phase estimate of the complex envelope of the amplitude-limited and phase-discriminated return has a noise term that is proportional to the quadrature component  $n_Q$  of the complex noise envelope. The differentiated (or differenced in the discrete case) phase-noise power spectral density is

$$S_{\dot{\phi}}(f) = \frac{\omega^2 S_{n_Q}(f)}{A^2} = \frac{\omega^2 S_n(f)}{2A^2},$$

where  $S_n(f) = \sigma^2/B_n$  is the power spectral density of  $n(t)$ . The noise power, or variance, of a complex noise sample is  $\sigma^2$  and the noise bandwidth is  $B_n$ . The output noise power at the modulation frequency  $f_m$  with a filter of bandwidth  $B_r$  is

$$N_0 = B_r S_{\dot{\phi}}(f_m) = \frac{B_r \omega_m^2 \sigma^2}{2B_n A^2}.$$

The differentiated signal power is just

$$S_0 = \frac{\beta^2 \omega_m^2}{4}$$

The ideal limiter/FM-discriminator output SNR for the glint-target case, which corresponds to the standard FM demodulation of a steady signal, in the high-input-SNR case becomes

$$\text{SNR}_{out} = \frac{S_0}{N_0} = \frac{\beta^2 B_n \text{CNR}}{2B_r}, \quad (13)$$

where the input SNR, which is equivalent to CNR in this case, is defined as  $\text{CNR} = A^2/\sigma^2$ . (Note that in this high-CNR case we can ignore spike noise, or click noise, in the FM-discriminator output.)

### Simulation

A simulation of both the spectrogram and FM-discriminator process was developed to verify the theory for these processes and to extend the performance results to the low-CNR regime [4]. In the simulation we generated a complex-envelope vector of 16,384 points with a complex sample rate of 80 kHz. This

vector length corresponds to a measurement interval of  $T_m = 0.2048$  sec, or an output frequency resolution of  $B_r = 4.883$  Hz (before amplitude weighting). The first FFT frequency bin size, or output bin resolution, must be smaller than the frequency deviation of the modulation signal, and the output centroid sampling rate should be at least twice as large as the corresponding largest vibration frequency in order for the simulation to satisfy the assumptions of the theoretical analysis.

The complex-envelope description of the target return included complex speckle noise, phase noise, and additive Gaussian LO shot noise with arbitrary bandwidth and variance as desired. Amplitude weighting and convolution of the signal-plus-noise vector was performed for sidelobe reduction and spectral containment. A three-term Blackman-Harris weighting function, or window, was used. This window has a 3-dB-bandwidth broadening factor of approximately 1.66 and a loss in processing gain of approximately 2.3 dB. In the following simulations, the spectrogram process used no frame averaging. An ideal limiting operation was used in the FM-discriminator process.

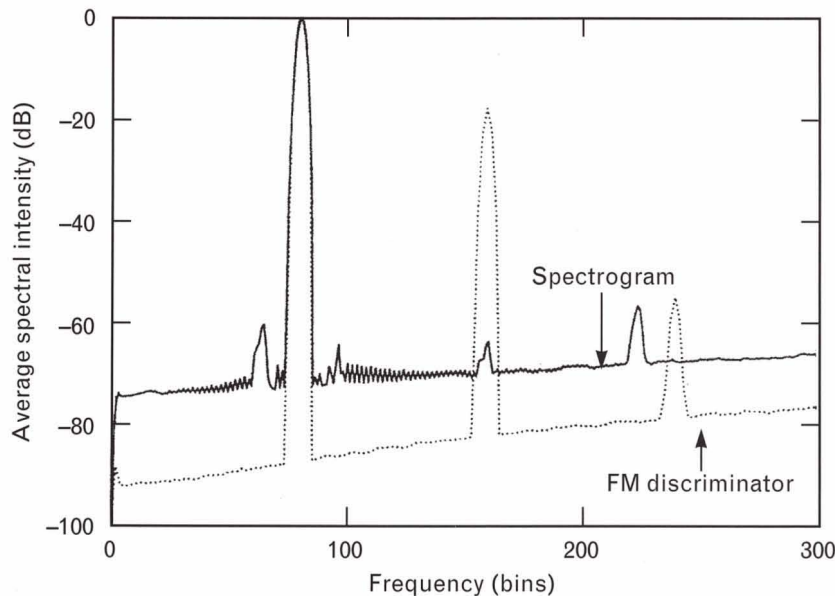


**FIGURE 4.** Average spectral intensity versus frequency for a single-tone glint-target vibration. The parameters are  $\beta = 25$ ,  $f_m = 195$  Hz,  $\text{CNR} = 30$  dB,  $B_n = 26.6$  kHz,  $B_r = 4.88$  Hz, and  $B_c = 2.5$  kHz. As we expect, the FM discriminator outperforms the spectrogram processor. The harmonics appear for the FM-discriminator processor because of the two-point differencing operation used to perform differentiation of the discrete data set.

Figure 4 shows the average output spectral intensities for a spectrogram-processed and an FM-discriminator-processed glint-target return. The actual output frequency is found by multiplying the frequency bin number and the 2.441-Hz zero-padded bin resolution. For this example the modulation frequency is 195 Hz, the FM modulation index is 25, the LO shot-noise bandwidth is 26.6 kHz, the IF bandwidth is 80 kHz, the process bandwidth out of the first FFT is 2.5 kHz, the frequency-resolution bandwidth is 4.88 Hz, the CNR is 30 dB, and the processing loss due to the Blackman-Harris weighting is 2.3 dB.

By using Equation 6 and including the processing loss, we determine the theoretical output SNR for the spectrogram demodulator to be 74.2 dB; from the figure we estimate the output SNR to be approximately 74 dB. For the FM discriminator, Equation 13 shows that the theoretical output SNR is approximately 90 dB, including the processing loss, while the simulation yields an estimate of approximately 88 dB. The approximate agreement between the theory and the simulation for the FM discriminator is within reason, given that the theory is based on assumptions of a

high CNR and a rectangular, or flat, IF spectrum.

In Figure 5 we show the spectrogram and FM-discriminator performance for a diffuse target, using the same parameters as for Figure 4. By using Equation 4 and including the processing loss, we determine the theoretical output SNR for the spectrogram demodulator to be 31.8 dB, while from the figure we estimate the simulation output SNR to be approximately 32.5 dB. For the FM discriminator, Equation 11 shows that the theoretical output SNR is 25.1 dB, including the processing loss, while the simulation yields an estimate of approximately 27.5 dB.

Figure 6 shows the spectrogram and FM-discriminator performance for a diffuse target with two-tone complex vibration. The modulation frequencies are 195 Hz and 122 Hz, with FM modulation indexes of 25 and 50, respectively. The LO shot noise and signal speckle bandwidths after weighting are 26.6 kHz and 13.28 kHz, respectively, and the CNR is 30 dB. The squared ratio of the frequency deviation of the two tones is approximately 1.56. Consistent with the theoretical expressions, the output SNR is approximately 2 dB higher for the first tone at 122 Hz.

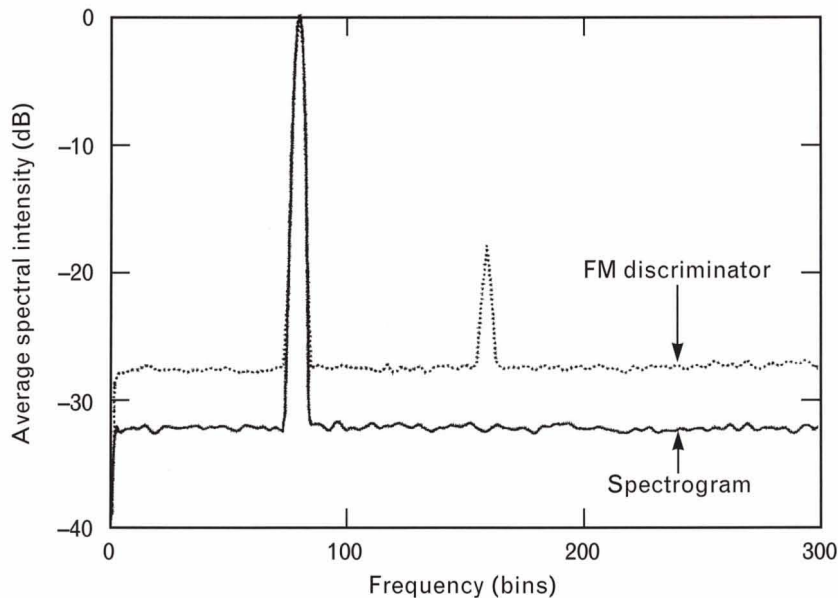


**FIGURE 5.** Average spectral intensity versus frequency for a single-tone diffuse-target vibration. The parameters are  $\beta = 25$ ,  $f_m = 195$  Hz, CNR = 30 dB,  $B_n = 26.6$  kHz,  $B_r = 4.88$  Hz,  $B_s = 6.64$  kHz, and  $B_c = 2.5$  kHz. In this case the spectrogram processor wins over the conventional FM discriminator on average by approximately 5 dB. This difference is to be expected because the diffuse target exhibits speckle-like behavior.

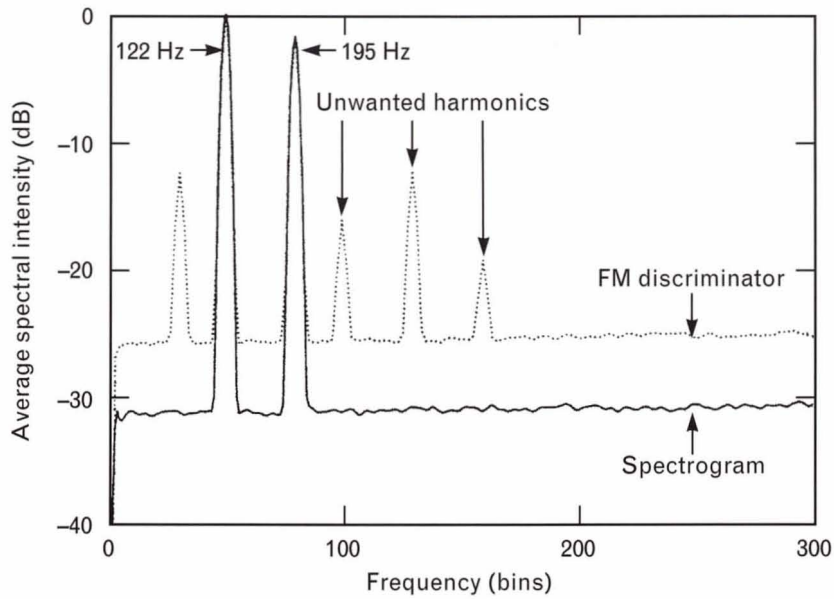


**FIGURE 6.** Average spectral intensity versus frequency for a diffuse target with a two-tone complex vibration. The parameters are  $\beta_1 = 50$ ,  $f_{m1} = 122$  Hz,  $\beta_2 = 25$ ,  $f_{m2} = 195$  Hz,  $\text{CNR} = 30$  dB,  $B_n = 26.6$  kHz,  $B_r = 4.88$  Hz,  $B_s = 13.28$  kHz, and  $B_c = 2.5$  kHz. Consistent with the results shown in Figure 5, the performance of the spectrogram processor is over 5 dB better than that of the FM discriminator. In addition, we see that the strengths of the two vibration modes are proportional to their frequency deviations.

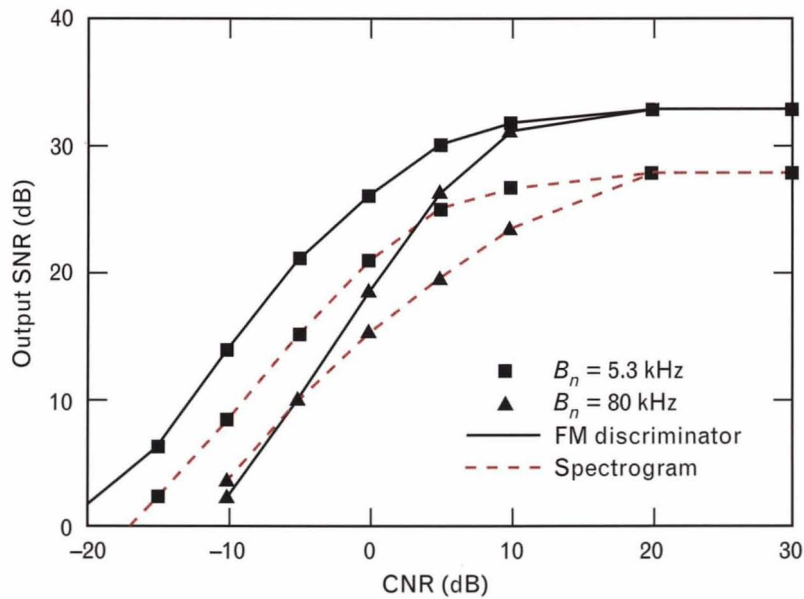


**FIGURE 7.** Output SNR as a function of the CNR for a diffuse-target return. The parameters are  $\beta = 25$ ,  $f_m = 195$  Hz,  $B_r = 4.88$  Hz,  $B_s = 6.64$  kHz, and  $B_c = 2.5$  kHz. We see that the spectrogram consistently outperforms the FM discriminator when the noise bandwidth is small (5.3 kHz) with respect to the IF bandwidth (80 kHz). When the noise bandwidth is much broader than the speckle bandwidth and when the CNR is relatively low, however, then the centroid variance is dominated by the noise in those frequency bins far from the important, or central, frequency bins containing the signal energy.

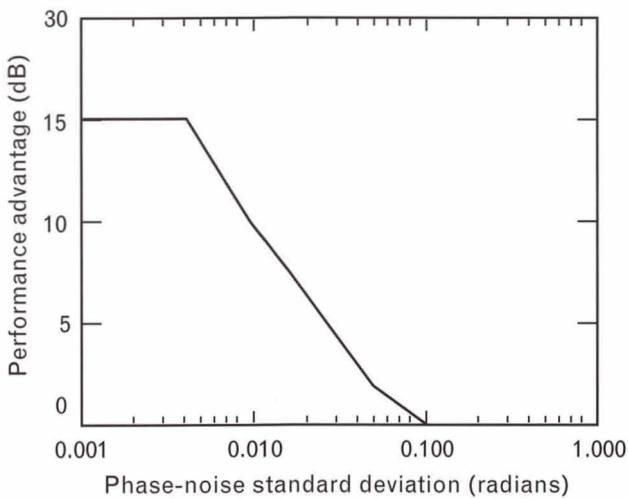


**FIGURE 8.** Performance advantage of the FM discriminator for a glint target as a function of the standard deviation of the phase noise. The simulation parameters are  $\beta = 25$ ,  $f_m = 195$  Hz,  $\text{CNR} = 30$  dB,  $B_n = 26.6$  kHz,  $B_r = 4.88$  Hz, and  $B_c = 2.5$  kHz. Notice that the performance advantage disappears well before the typical deviation of 1 radian for a commercial  $\text{CO}_2$  laser.

Figure 7 shows the output SNR performance for the spectrogram and the FM-discriminator processes

with a diffuse-target return as a function of the CNR for two different noise bandwidths. The narrowband noise bandwidth is 5.3 kHz and the wideband shot-noise bandwidth is 80 kHz. The figure shows that the spectrogram consistently outperforms the FM discriminator except in the case of simultaneously low CNR and wideband LO shot noise. If the noise is narrowband, then the spectrogram process is better at all values of CNR.

For a pure glint target with no phase noise, the FM discriminator outperforms the spectrogram process. Even a small amount of narrowband LO phase noise, however, will eliminate this advantage. Figure 8 shows the relative performance between the two processes for the glint target of Figure 4 as a function of the standard deviation of the phase noise. The phase-noise 3-dB bandwidth of 1.6 kHz and a nominal standard deviation of 1 radian is considered typical for a commercial  $\text{CO}_2$  laser. The performance advantage of the FM discriminator disappears for a phase-noise standard deviation of 0.1 radians (or  $5.7^\circ$ ). Note that we chose this high modulation index and high-CNR case to maximize and accentuate the performance dif-

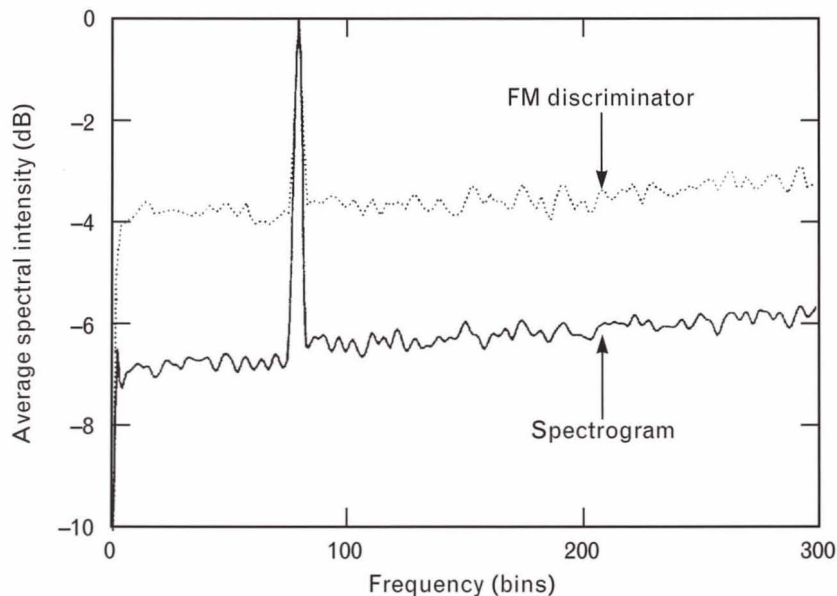


**FIGURE 9.** Average spectral intensity versus frequency for a single-tone small-frequency-deviation diffuse-target return. The parameters are  $\beta = 1.25$ ,  $f_m = 195$  Hz,  $\text{CNR} = 10$  dB,  $B_n = 80$  kHz,  $B_r = 4.88$  Hz,  $B_s = 6.64$  kHz,  $B_c = 2.5$  kHz,  $\sigma_f = 1$ , and  $B_p = 1.6$  kHz. Even for frequency deviations that are small (244 Hz) compared to the frequency bin size  $B_c$  (2.5 kHz) of the centroid estimator, the spectrogram still outperforms the FM discriminator.

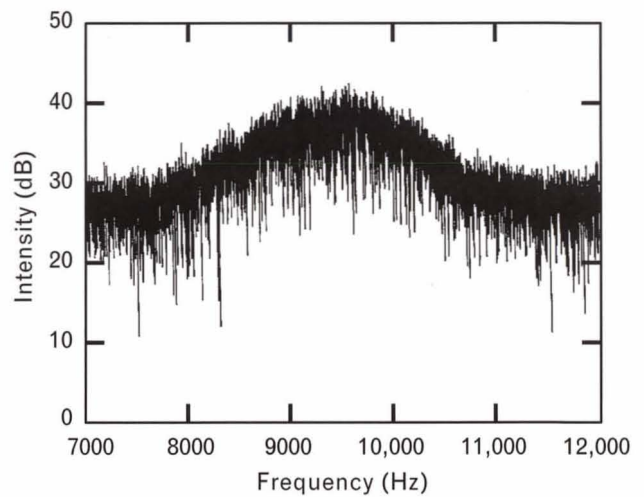
ference between the two processes. Of course, the phase-noise effect is reduced significantly in offset-homodyne systems when the target range is short [5].

Figure 9 shows the relative performance of the two processes in the small modulation index, or small frequency deviation, case for a diffuse target with a moderate amount of phase noise and at a CNR of 10 dB. Phase noise is included with a 3-dB bandwidth of 1.6 kHz and a standard deviation of 1 radian. We chose the single-tone frequency deviation of 244 Hz to be a small fraction of the frequency bin size ( $B_c$ ) of the first FFT in the spectrogram process. As the figure shows, the spectrogram process for this example still has a 3-dB advantage. Increasing the single-tone frequency deviation to 488 Hz results in about a 4-dB spectrogram advantage.

#### LVS Measurement Data

We used an LVS developed by North American Rockwell, Inc. to collect short-range (1 to 2 km) vibration data on nautical objects, including a commercial cruise liner and several small boats in San Diego harbor. The LVS had an average power of 5 W and a transmit/receive aperture of 5 cm, and it operated at a 10.6- $\mu$ m wavelength. The typical beam spot size on the target was 20 to 30 cm. The offset-homodyne-detected return signals were translated to a 10-kHz IF and recorded with a Honeywell 101 analog tape recorder.

Later, at Lincoln Laboratory, we played back the analog tapes and digitized the recorded signals at a 100-kHz rate. The digitized signals were then pro-



**FIGURE 10.** Typical measured IF spectrum. The speckle bandwidth is approximately 1 kHz at a 10-kHz IF.

cessed with both the digital FM discriminator and spectrogram algorithms for comparison. Figure 10 shows a plot of the IF spectrum of a typical return signal, measured over a one-second interval. From the figure we see that the 3-dB speckle bandwidth is approximately 1 kHz. Table 2 summarizes the digital signal processing parameters we used to process the measurement data for the CW spectrogram and the digital FM discriminator.

#### System Noise

When collecting vibration data in San Diego harbor, we used a nearby jetty, which served as a motionless non-vibrating object, to calibrate the LVS. Any systematic vibration errors in the LVS show up as tonal

**Table 2. Spectrogram and Digital FM-Discriminator Processing Parameters\***

| <i>Spectrogram</i>                          | <i>FM Discriminator</i>              |
|---|--------------------------------------|
| 160- $\mu$ sec coherent processing interval | Ideal limiting                       |
| 5-spectrum average                          | 100,000 samples per measurement      |
| Center-of-mass centroid                     | Output 0–50 kHz with 1-Hz resolution |
| 1250 centroid samples (second-stage FFT)    |                                      |
| Output 0–625 Hz with 1-Hz resolution        |                                      |

\* 10-kHz IF carrier frequency, 100-kHz sampling frequency, and one-second measurement interval

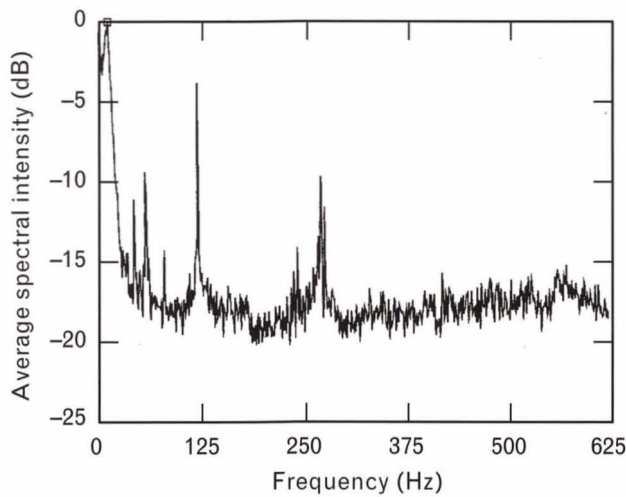
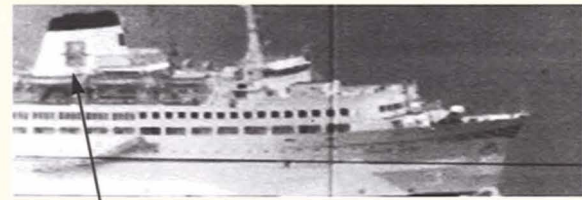


**FIGURE 11.** The LVS system noise, or response to a steady non-vibrating object. This response was formed by averaging several minutes of one-second spectra that were computed by processing the returns from a nearby jetty.

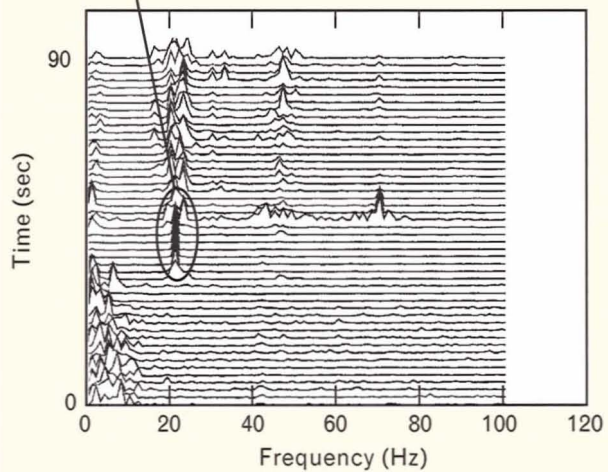
resonances in the system response. Phase noise produces a higher noise floor in the output vibration spectrum. Figure 11 shows the system noise of the LVS, based on the average of several minutes of one-second jetty vibration spectra. The system response has a high noise level in the 0-to-20-Hz frequency band, and substantial tonal responses at frequencies of 42, 55, 60, 120, 240, and 270 Hz.

The average spectral intensity obtained from a series of one-second stationary-object measurements can be used as a calibration, or *normalization*, curve for object measurements that occur during a relatively short time after the calibration. If the systematic noise process is stationary, and constant for some of the tonals, then dividing the observed object vibration spectrum by the calibration curve will reduce or de-emphasize the undesired tonals and the regions of high-level phase noise. This normalization tends to introduce blind spots at the unwanted tonal frequencies, however, and reduces the sensitivity in the regions of high phase noise. Also, a distortion of the vibration spectrum can occur because the gain is increased for frequencies at which the calibration curve, or systematic noise level, is low.

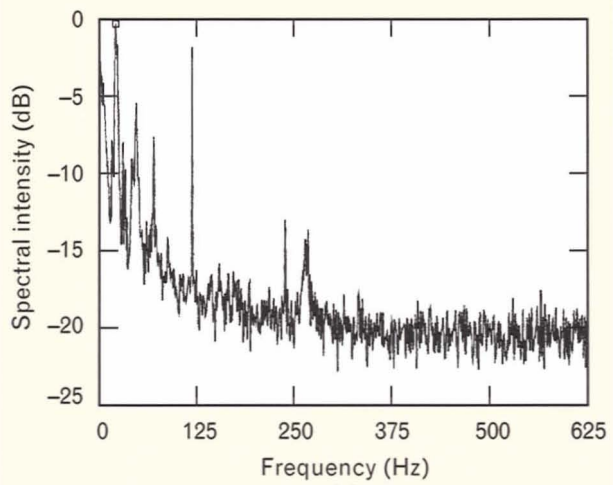
A more sophisticated calibration technique to suppress noise would be to measure the unwanted LVS platform vibrations with accelerometers placed in



(a)



(b)



(c)

**FIGURE 12.** Vibrational spectra for (a) a commercial cruise liner. (b) The spectral history is displayed in one-second snapshots as a function of the relative measurement time. (c) Also shown is the time-averaged spectral intensity of all the one-second spectra. The arrow in the photo of the cruise liner in part a indicates where the LVS was pointing when the spectral peaks occurred.

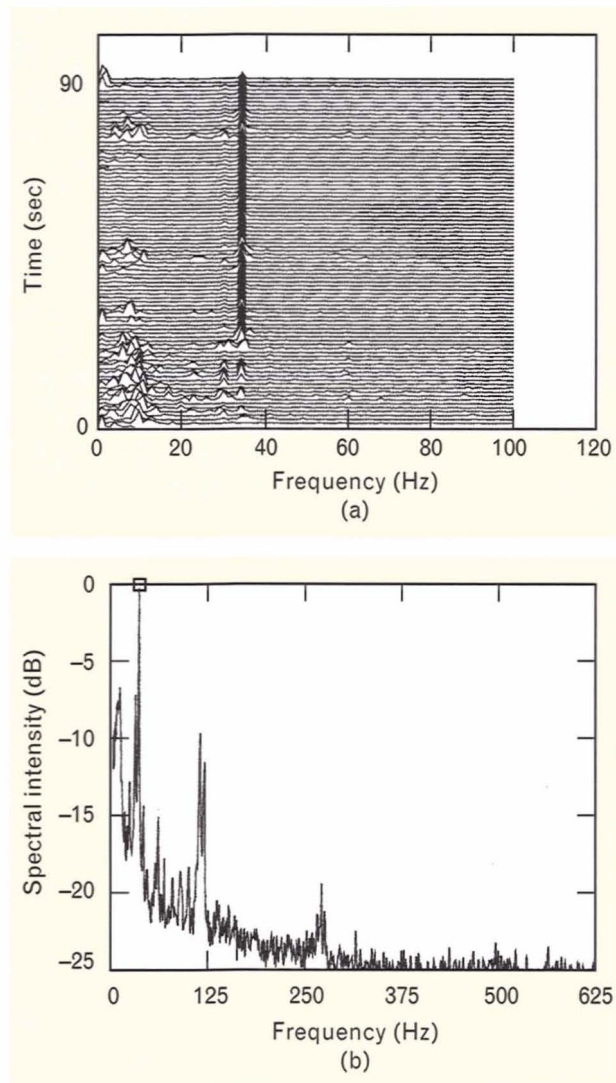


**FIGURE 13.** Vibrational spectra for a typical small boat. (a) The time-invariant spectral peak over the measurement interval is probably due to strong engine vibrations. The consistency can be attributed to both the small size of the boat—i.e., all parts are vibrating equally—and a constant engine RPM.

each of the three dimensions of the LVS, and then use these reference accelerometer signals to cancel the unwanted vibrations, or systematic noise, adaptively.

#### *Spectrogram-Processed Spectra Examples*

Figures 12 and 13 show the spectrogram-processed vibrational spectra for a commercial cruise liner and for a small boat, respectively. Each figure has a spectral-time-intensity (STI) plot that shows how the vibrational spectrum evolves over the measurement in-

terval. This plot can be interpreted as the spectral history of the vibrational modes of the object. Each line of the STI plot represents on a linear scale the intensity of the vibrational spectrum as a function of vibration frequency from 0 to 100 Hz, as obtained during a one-second measurement interval. Consecutive one-second vibrational spectra over the total measurement interval make up the STI plot.

Each figure also shows a plot of the average spectral intensity versus frequency on a dB scale over the entire output frequency band, where the average is computed by using all of the one-second vibrational intensity spectra that are collected over the entire measurement interval. Transient features tend to be washed out or deemphasized in the averaged spectrum, while persistent or long-lasting features tend to be enhanced or magnified.

We see from these two figures that both vessels exhibit some vibrational responses that are distinguishable from the undesired tonals in the system-noise response caused by platform vibrations and systematic errors, as shown in Figure 11. Notice in Figure 12 that the strongest tonals for the cruise-liner data appear when the beam is placed on the ship funnel area where the vibrations are strongest.

The platform vibrations and ground-loop problems caused a superficial spectral richness in the measured spectra. Small vibration signal amplitudes occurred because of the calm waters and low-power operation of the boats in the bay. Longer ranges reduce the spatial dependency of the vibration responses, and at the same time the speckle fading rate increases with a larger beam spot size.

In general, the spectrogram process was found to perform better than the ideal-limiter/digital-FM-discriminator process. Figure 14 shows the one-second-averaged vibrational spectra obtained from several minutes of measurements for both processes from a typical vessel. Notice that the spectrogram process appears to perform better because the spectral noise floor is lower. This lower noise floor results in a greater dynamic range of the spectrogram-processed data. Although the overlaid plots do not reveal the differences in spectral peaks, the spectral peaks are also slightly higher for the spectrogram process. In Figure 14, the unwanted spectral peak at 120 Hz is approximately 2

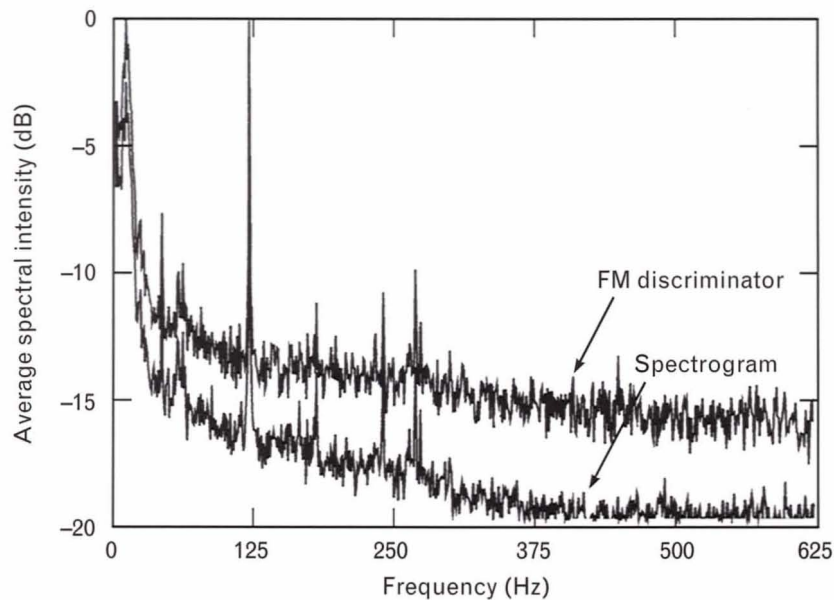


**FIGURE 14.** Comparison of the average vibrational spectra obtained by using the spectrogram and digital FM-discriminator processes for a typical vessel. The higher peaks and lower noise floor of the processed data of the spectrogram give it an advantage of 4 to 5 dB.

dB higher for the spectrogram process. This higher peak, in combination with the lower noise floor, gives the spectrogram process a 4-or-5-dB advantage. Several other vessels were compared and the results were similar. In addition, the spectrogram process is less computationally intensive than the digital FM discriminator.

### Ground-Based LVS Measurements of On-Orbit Satellite Vibrations

We used the spectrogram technique to process LVS measurements of the LACE satellite (NORAD object 20496) [2]. Such *in situ* measurements of orbiting structures provide valuable information regarding structural dynamics and require only simple modifications to the existing structure (e.g., the addition of retroreflectors). While sophisticated mechanical simulation programs to evaluate in-space dynamics exist, *in situ* measurements of satellite vibration are rare; to date only one previous experiment has been dedicated to collecting on-orbit vibration data [6]. The experiment, known as the Solar Array Flight Experiment (SAFE), used on-board sensors to measure boom vibrations during a period of eighteen hours. While this experiment provided considerable data, a larger data-

base is required to develop and validate structural dynamics models.

The primary mission of the LACE satellite, which is illustrated in Figure 15, was the evaluation of low-power atmospheric compensation techniques. The LACE satellite, which was launched on 14 February 1990 into a 540-km-altitude circular orbit of 43° inclination, consists of a massive body and three deployable/retractable booms of maximum length equal to 45.7 m (150 ft). Constant-rate boom deployment/retraction maneuvers are remotely controlled through a ground-based telemetry link. To facilitate ground-based coherent-infrared LVS measurements, 3.8-cm infrared germanium retroreflectors were mounted on the retroreflector boom, the satellite body, and the balance boom, as shown in Figure 15.

### Description of Firepond CO<sub>2</sub> LVS

Figure 16 depicts a simplified block diagram of the coherent chopped-CW infrared LVS used to collect satellite vibration data. This LVS is based on a master-oscillator (MO) power-amplifier configuration operating on the P<sub>1</sub>(20) line of <sup>12</sup>C<sup>16</sup>O<sub>2</sub> ( $\lambda = 10.59 \mu\text{m}$ ) [7]. The MO and LO are a pair of frequency-offset-locked ( $\Delta f = 10 \text{ MHz}$ ) CO<sub>2</sub> lasers operating CW. The

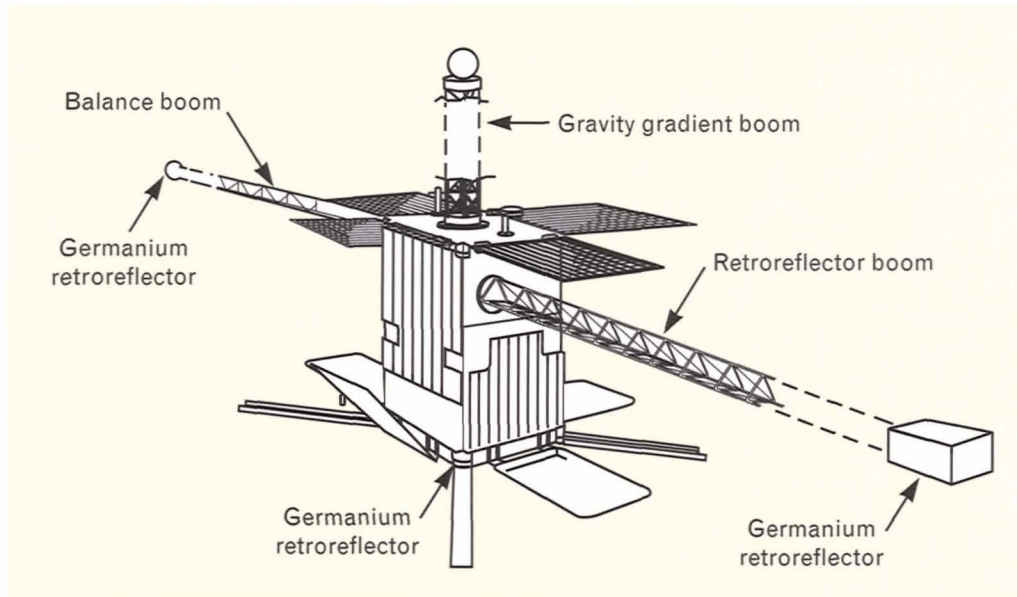


**FIGURE 15.** Simplified representation of the LACE satellite. Angle tracking on the satellite is maintained with a visible retro array located on the retroreflector boom tip. The three deployable/retractable booms each have maximum extent of 150 ft. A CO<sub>2</sub> LVS was used to measure the relative vibration between the germanium retroreflector located on the satellite body and the retroreflector located on the retroreflector boom tip.

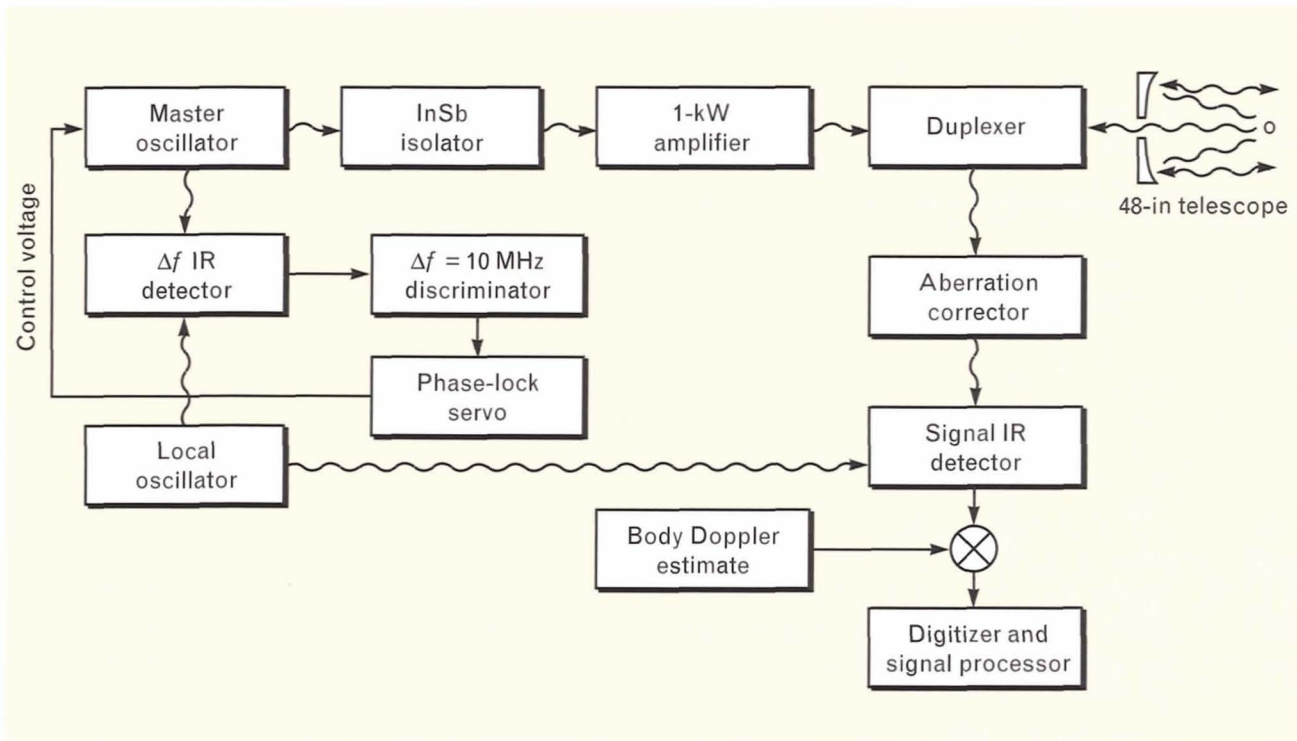


**FIGURE 16.** Simplified block diagram of the pulsed CW CO<sub>2</sub> laser radar facility. The LVS is based on a master-oscillator power-amplifier configuration in which the master oscillator and local oscillator are frequency-offset locked with  $\Delta f = 10$  MHz. The return signal is mixed with the local oscillator on the IR detector.

mutual long-term stability of the laser pair has been measured to be better than 1 Hz [8].

The MO output passes through an InSb isolator to the first tube of a linear-discharge axial-flow 1-kW power amplifier. The amplified output is chopped to form 3.2-msec pulses at a pulse repetition frequency (PRF) of 62.5 Hz. The resultant output converges to a focus at the receiver duplexer and then passes to a 1.2 m (48 in) Cassegrain telescope fitted with a high-speed secondary mirror for precision angular tracking. The full width at half maximum (FWHM) of the near-diffraction-limited transmit beam is approximately 10  $\mu$ rad, resulting in a nominal 5-m FWHM footprint at a range of 500 km. The nominal peak transmit power is 600 W.

The received signal, which contains both the gross-target Doppler shifts and vibration-induced frequency shifts, is mixed with the 10-MHz offset LO. The offset-heterodyne-detected signal is then converted to a fixed IF frequency by mixing the return with an estimate of the body Doppler frequency. This estimate can be obtained from a predicted satellite orbital-track file, a real-time estimate derived from the Doppler return signal, or a real-time frequency estimate obtained from the Millstone L-band tracking radar. After further mixing to generate a baseband signal, the complex in-phase and quadrature signal is digitized by using a 1.2-MHz A/D converter and stored for subsequent processing. The 1.2-MHz A/D converter, which digitizes a 3.4-msec segment of the received signal, is triggered based on the predicted round-trip transit time.

The stability of the entire laser radar system, including round-trip atmospheric propagation effects, was obtained by estimating the frequency spread associated with a single retroreflector located on the GEOS III satellite (NORAD object 7734) [8]. The results suggest short-term stability better than  $1.5 \times 10^{-13}$  for a 7-msec round-trip duration. Doppler resolution, however, is limited by the 3.2-msec pulse duration; the radar achieves a Doppler frequency resolution of approximately 300 Hz, corresponding to a velocity resolution of 1.6 mm/sec at  $\lambda = 10.59 \mu\text{m}$ . A nominal resolution of 2.4 mm/sec is obtained when the pulse is Hamming weighted prior to Fourier transformation.

Satellite tracking was accomplished with the aid of two additional radar systems: a pulsed CW Ar<sup>+</sup> laser multiplexed and boresighted with the CO<sub>2</sub> beam and the Millstone L-band tracking radar. The pulsed Ar<sup>+</sup> laser, operating at a PRF of 62.5 Hz, was used in conjunction with a quad monopulse photon-multiplier-tube detector array to obtain a precise angular track on a visible retroreflector array located on the forward boom of the LACE satellite. The Millstone L-band radar supplied real-time target state-vector information for target acquisition and tracking. In particular, target range-rate (Doppler) information was used to help acquire and track the LACE satellite. A passive 24-in visible tracker was used to acquire the target in angle; the target was then observed during terminator passes—i.e., the sun-illuminated satellite was observed against a dark night sky.

#### *Experimental Methods*

We conducted a series of experiments to measure the forced vibrations present during boom retraction and the free-damped vibrations present subsequent to boom retraction. Observations were obtained within a 5 m (minimum FWHM) footprint that included both the retroreflector-boom and satellite-body retroreflectors; the balance-boom retroreflector was fully extended to preclude observation. (The projection of the extended retroreflector boom onto the cross-range area defined by the laser radar line of sight must lie within the laser radar footprint. This requirement, in conjunction with the geometry of the satellite trajectory with respect to the radar line of sight, resulted in measurements with the boom extended beyond 5 m.) Observation windows for each pass were predetermined by NORAD. Prior to the onset of the allowed window, the retroreflector boom, which was initially set at 24.4 m (80 ft), was retracted to 4.6 m (15 ft). The retraction was timed such that the boom stopped within the allowed observation window.

Boom vibration measurements were obtained during 7, 8, and 10 January 1991. The data consisted of 3.2 msec of digitized in-phase and quadrature data received at a nominal 62.5-Hz rate during temporal observation windows on the order of 100 sec. The quantity of interest—the quasi-instantaneous velocity between the illuminated retroreflectors—is encoded

in both the amplitude and frequency of the in-phase and quadrature data. In particular, the time-varying signal amplitude, or envelope, is a result of the coherent interference between two flood-illuminated retroreflectors. In this case, the amplitude modulation frequency is proportional to the relative velocity component between the two retroreflectors projected onto the LVS line of sight. Alternatively, the net Doppler shift of each retroreflector (corresponding to the Doppler shift induced by the net projected retroreflector velocity relative to the site LO) is imparted to the reflected signal. In this case, the projected relative velocity between retroreflectors may be inferred by observing the difference between frequencies associated with the spectral peaks.

The amplitude and frequency encoding of the desired information impacts both the signal processing and the possible receiver architecture. The analysis presented here is based on frequency-encoded velocity information; the power spectrum of the complex in-phase and quadrature time data is computed for each 3.2-msec digitized pulse (i.e., the magnitude squared of the complex 4080-point FFT is computed for each received pulse). Each power spectrum contains two peak returns with associated difference frequency  $\Delta f$  given by the expression

$$\Delta f = \frac{2v_r}{\lambda},$$

where  $v_r$  and  $\lambda$  correspond to the relative velocity along the LVS line of sight and laser wavelength, respectively. The desired boom vibration is obtained through a spectral analysis of the time evolution of the difference velocity between the two retroreflectors.

The relevant component of boom-tip motion is due to complex three-dimensional time-varying vibration modes. What the LVS ultimately measures, however, is the one-dimensional projection of the net boom-tip velocity relative to the satellite body onto the LVS line of sight. In general, this relative velocity between the boom tip and satellite body consists of three components: (1) the desired vibration-induced velocity, (2) the retraction/deployment velocity, and (3) the velocity induced by rigid-body motion between the retroreflector boom tip and the satellite body.

By using detailed information regarding the satellite trajectory, we can compute the satellite orientation with respect to the LVS line of sight; in addition, with knowledge of the boom deployment/retraction rates, we can infer the vibration-induced component. These compensated vibration-mode data collected from a given satellite pass represent mode data projected onto the LVS line of sight. Theoretically, the three-dimensional modal structure can be derived by applying reconstruction-from-projection techniques to a set of projection data obtained at multiple aspect angles. The practical implementation of this reconstruction, which depends on both a large viewing angle and the repeatability of a given experiment, is not addressed here.

On the basis of the above considerations, we used the following modified spectrogram method to obtain the projected retroreflector boom-tip velocity as a function of time: (1) compute the power spectrum of each pulse; (2) for each spectrum, detect two peak returns associated with the retroreflector boom tip and body retroreflectors; (3) estimate the difference frequency (relative velocity) between retroreflector returns; and (4) compensate for retroreflector-boom retraction rate and changing satellite aspect-angle effects.

The above modified spectrogram approach measures relative target motion only; as the IF spectrum width is estimated, the technique ultimately extracts the amplitude-encoded or autodyne signature [3]. With the compensated boom-tip velocity computed according to the above steps, the modal frequency analysis proceeded as follows. For data collected during the retroreflector-boom retraction maneuver, a simple time-frequency analysis based upon a short-time Fourier-transform technique is employed. In this case, the power spectrum of a moving Hamming window of temporal duration equal to 24 sec (corresponding to 1500 samples at the 62.5-Hz PRF) is computed at intervals of 0.1 sec. The effective frequency resolution ( $\approx 0.06$  Hz) and time resolution ( $\approx 17$  sec) were selected based on a qualitative analysis of the data; more sophisticated time-frequency analysis techniques are not discussed here. A conventional Fourier spectral analysis was used to process data subsequent to the boom maneuver.

### Results and Discussion

Data were collected during terminator passes during 7, 8, and 10 January 1991. Only data from days 8 and 10 are presented here. Measurements acquired during day 8 contain approximately one hundred seconds of data during the boom retraction with another thirty-five seconds of post-boom retraction data. These data are used to obtain a time-frequency analysis during the boom deployment period and a modal analysis for data subsequent to the retraction. Data from day 10 contain about twenty seconds of data during the boom retraction and sixty seconds of data subsequent to boom retraction. We note here that the receiver generates artifacts near the zero-Doppler (or turn-around) point in the trajectory, which in the case of day 10 occurred just prior to the boom stopping. As a

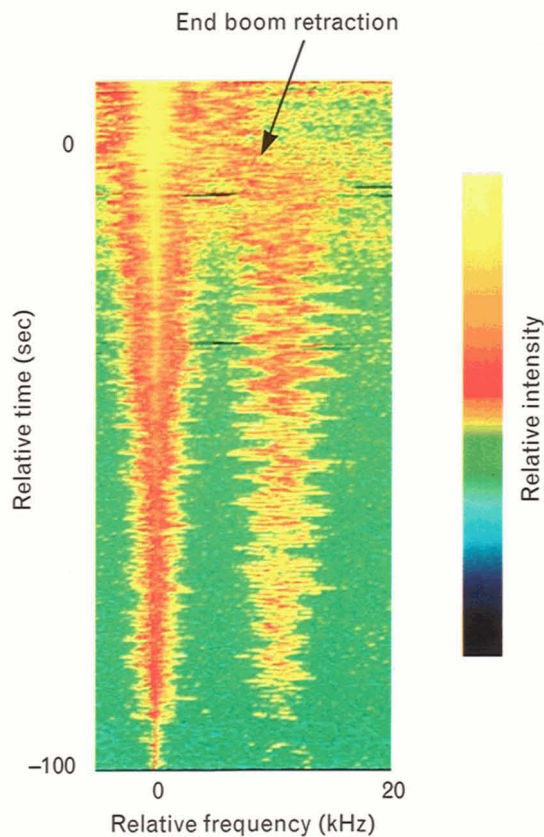


**FIGURE 17.** Doppler-time-intensity representation of data acquired on 8 January 1991. The data have been aligned to the peak return. Vibration effects are clearly evident. The step in the oscillatory trajectory coincides with the termination of boom retraction.

result, data from day 10 have been analyzed for the presence of free vibration modes only. (While data collected on day 7 are not presented in this article, the results are completely consistent with data collected on day 8.)

### Vibrations during Boom Retraction

The power spectra data associated with day 8 are shown in a Doppler-time-intensity (DTI) format in Figure 17. Here the power spectra from each 3.2 msec of digitized data are aligned and displayed along the vertical time axis. The horizontal axis corresponds to Doppler frequency (or velocity). The relative motion between the two retroreflectors manifests itself as an oscillatory curve in the DTI. For example, the end of the boom retraction is indicated by the step in the curve, and the presence of high-frequency vibration modes are apparent during the retraction.

The result of peak detection and subsequent temporal filtering yields the data shown in Figure 18(a). (Median and low-pass filtering were employed.) Here the projected, or apparent, relative velocity between the boom tip and satellite body is plotted against time, relative to the termination of the boom retraction maneuver. The combined rigid-body-and-boom retraction velocities are superposed onto the measured values.

The residual vibration-induced boom-tip velocity shown in Figure 18(b) is obtained after subtracting out the non-vibrating velocity component and scaling the result to compensate for aspect-angle variations during the observation window. A preliminary frequency analysis of the time-series data is performed by Hamming-weighting the data over the entire temporal window and computing the power spectrum. (The nominal resolution of the resultant spectrum is 0.01 Hz.) The result, presented in Figure 18(c), indicates the presence of multiple vibration frequencies.

The spectral peak at 1.03 Hz in Figure 18(c) is close to the expected driving frequency of the boom retraction mechanism. The spectral peak at 0.12 Hz is close to the predicted free-damped vibration mode of 0.13 Hz, and the spectral peak at 0.28 Hz is relatively close to the predicted vibration mode of 0.32 Hz (see Table 3 below). The slight bias between the observed and predicted values can be attributed, in part, to the

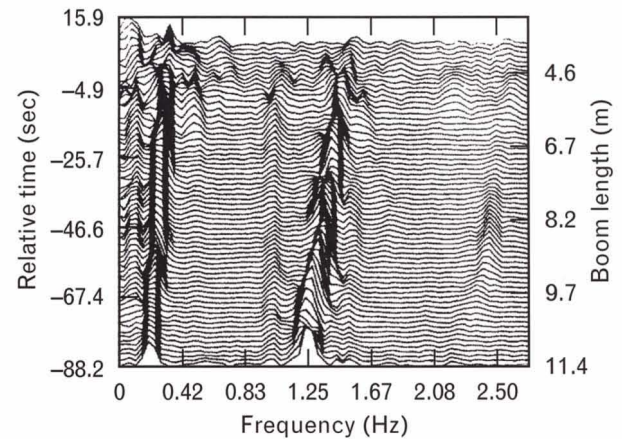
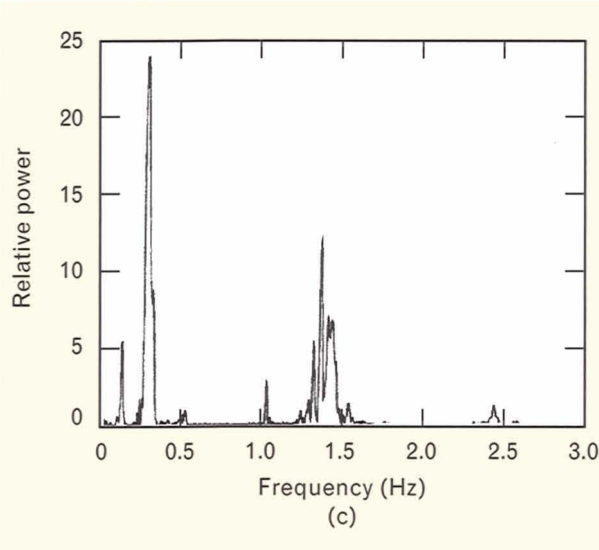
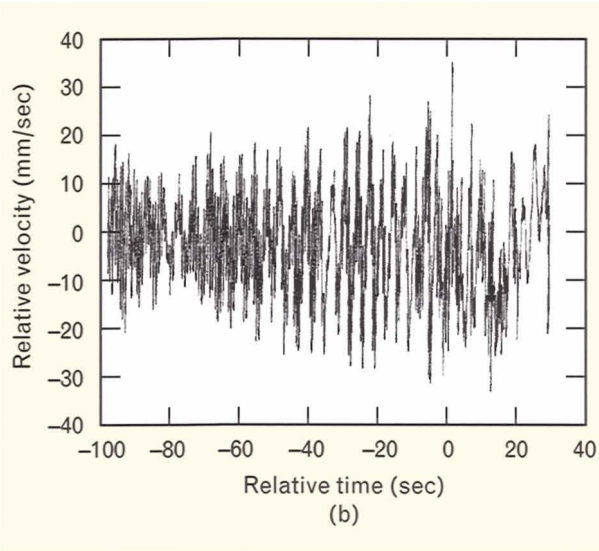
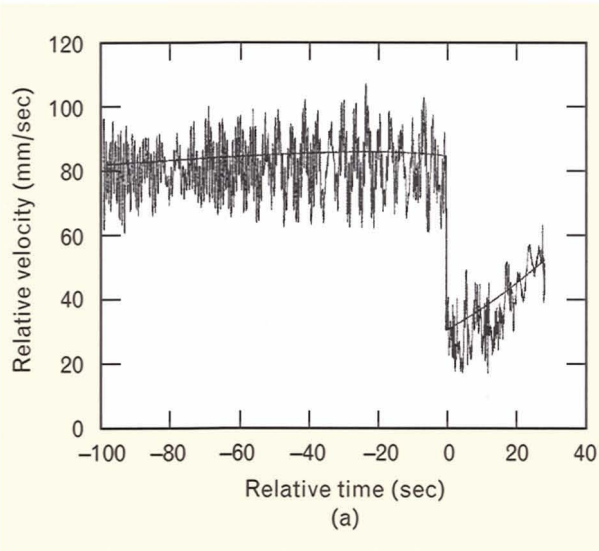


**FIGURE 19.** Time-frequency analysis of vibration data obtained from the LACE satellite on 8 January 1991. Modes associated with the retroreflector boom increase in frequency as the boom retracts. The constant frequency (1.03 Hz) can be associated with the drive mechanism.

fact that this 0.28-Hz mode appears to increase in frequency as the boom is retracted, a result suggested by the time-frequency analysis described in the next paragraph. The remaining modes have not been well modeled and represent a new observation regarding on-orbit boom vibration dynamics.

Figure 19 presents the time-frequency analysis of the data from day 8. Represented in this way, the data clearly indicate that modes in the 0.28-Hz regime and in the higher 1.25-Hz regime increase in frequency as the boom retracts. The figure also indicates the relative stability of the 1.03-Hz mode, a result consistent with the behavior of a constant-rate drive mechanism.

#### *Vibrations Subsequent to Boom Retraction*

We used conventional Fourier spectral analysis to estimate vibration modes during the post-boom-retraction phase of data collected on 8 January 1991 and 10 January 1991. Results for the measured modal frequencies and damping factors are given in Tables 3 and 4, respectively.

The results indicate reasonable agreement between

**FIGURE 18.** (a) Measured retroreflector boom-tip velocity relative to the line of sight, and predicted velocity due to boom retraction and change in aspect angle. (b) Compensated vibration-induced retroreflector boom-tip velocity relative to the line of sight. (c) Hamming-weighted power spectra of compensated velocity data.

measured and predicted modal frequencies. Measurements indicate, however, the presence of a mode at ~0.5 Hz that was not predicted. This additional mode could be due to incomplete modeling or nonlinear dynamics, or both. The relatively large difference between modal damping-factor estimates can be attributed to the fact that mode amplitudes are more sensitive than modal frequencies to satellite orientation, and are thus more sensitive to bias errors introduced by the velocity-compensation algorithm.

### Summary and Conclusions

We derived theoretical expressions for output SNR for diffuse-target vibrations for the spectrogram and the conventional FM-discriminator processes. Theoretical results suggest that the CW spectrogram process provides approximately 6-dB better performance than the conventional FM discriminator in the high-CNR diffuse-target case. We also derived theoretical

expressions for the glint, or steady, target vibrations. Numerous simulation results were presented that support the theory and extend the results to the low-CNR regime. We investigated other deleterious effects such as LO phase noise and small frequency deviations via the simulation. The theoretical and simulation results showed general agreement. The simulation showed that the spectrogram process provides approximately 4-to-6-dB better performance over the entire -20-dB-to-30-dB CNR range, except for the case in which the LO shot noise is broadband and stronger than the carrier. The advantage of the spectrogram for demodulation of diffuse-target vibrations is diminished by 1 to 2 dB with small frequency deviations. We found that the FM-discriminator advantage for glint-target vibrations, or standard FM demodulation, disappears with a relatively small amount of LO phase noise.

The spectrogram processing method was shown to

**Table 3. Predicted and Measured Modal Frequencies**

| <i>Predictions (Hz)</i> | <i>Measurements (Hz)</i> |                        |
|-------------------------|--------------------------|------------------------|
|                         | <i>8 January 1991</i>    | <i>10 January 1991</i> |
| 0.02                    | —                        | 0.02 ± 0.02            |
| 0.13                    | 0.12 ± 0.04              | 0.12 ± 0.02            |
| 0.32                    | 0.32 ± 0.04              | 0.33 ± 0.02            |
| —                       | 0.52 ± 0.04              | 0.51 ± 0.02            |

**Table 4. Measured Modal Damping**

| <i>Observed Modal Frequency (Hz)</i> | <i>Measurements (Percent)</i> |                        |
|--------------------------------------|-------------------------------|------------------------|
|                                      | <i>8 January 1991</i>         | <i>10 January 1991</i> |
| 0.02                                 | —                             | 1.39 ± 2.26            |
| 0.1                                  | -0.35 ± 0.35                  | 2.10 ± 0.30            |
| 0.3                                  | 1.11 ± 0.05                   | 2.00 ± 0.30            |
| 0.5                                  | 4.59 ± 0.26                   | 10.80 ± 1.02           |

have better performance than the digital FM discriminator (with ideal limiting) processing method when the Rockwell LVS measurement data were processed. The performance improvement in terms of output SNR was approximately 4 to 5 dB.

We used a modified spectrogram technique to process measured satellite-vibration data. Analysis of the LVS data indicated the presence of complex vibration modes during boom retraction. These data could prove useful in the development and validation of the next-generation modeling programs capable of accommodating a continuous excitation source. The measured steady-state vibrations were found to agree well with predictions, with the exception that measurements indicated the presence of an additional vibration mode not previously predicted. These data represent the first observations of satellite vibration modes from a ground-based LVS.

#### **Acknowledgments**

The authors gratefully acknowledge the assistance of D. Adams, E. Christiansen, M. Craig, J. Daley, J. Greene, M. Matei, G. Peck, A. Ruscitti, J. Spinks, A. Stein, L. Swezey, and the rest of the Firepond Family for taking care of laser radar operations. We also gratefully acknowledge the LACE operation and control facility for the coordination and implementation of LACE boom maneuvers, K. Varmaa for coordinating LACE flight operations, R. Sasiela for introducing Naval Research Laboratory to the Firepond laser radar, W. Schollenberger for programming assistance,

W. Guerin and C. Summers for their contributions toward collecting the Rockwell LVS data, and Rockwell International's Autonetics Strategic Systems Division for their cooperation. Finally, we would like to thank W. Keicher, L. Sullivan, and B. Edwards of Lincoln Laboratory for their support and encouragement, and the Department of the Navy and the Strategic Defense Initiative Office for sponsoring this effort.

---

---

## REFERENCES

1. A.L. Kachelmyer and K.I. Schultz, "Spectrogram Processing of Laser Vibration Data," *SPIE* 1936, 78 (1993).
2. K.I. Schultz, "Ground-Based Laser Radar Measurements of Satellite Vibrations," *Appl. Opt.* 31, 7690 (1992).
3. K.I. Schultz, D.G. Kocher, J.A. Daley, J.R. Theriault, J. Spinks, and S. Fisher, "Satellite Vibration Measurements with an Autodyne CO<sub>2</sub> Laser Radar," *Appl. Opt.* 33, 2349 (1994).
4. A.L. Kachelmyer, "Evaluation of Spectrogram Processing of Laser Vibration Signals via Computer Simulation," *Proc. Int. Conference on Lasers—LASERS '93, South Lake Tahoe, Nevada, 6-9 December 1993*.
5. R.S. Eng, C. Freed, R.H. Kingston, K.I. Schultz, A.L. Kachelmyer, and W.E. Keicher, "The Effects of Laser Phase Noise on Laser Radar Performance," *Proc. Int. Conference on Lasers—LASERS '92, Houston, Texas, 7-10 December 1992*.
6. Lockheed Missiles and Space Co. "Solar Array Flight Experiment Final Report," Marshall Space Flight Center, Huntsville, Ala. Contract NASA-31352, Report No. LMSC- F087173, (1986).
7. L.J. Sullivan, "Infrared Coherent Radar," *SPIE* 227, 148 (1980).
8. C. Freed, "Ultrastable Carbon Dioxide (CO<sub>2</sub>) Lasers," *SPIE* 709, 36 (1986).

## APPENDIX: CENTROID VARIANCE CALCULATION

ASSUME THAT  $N$  frequency bins containing both signal and noise are centered at the origin. The centroid estimate  $c$  is defined as

$$c = \frac{\sum_i x_i r_i}{\sum_i r_i},$$

where  $x_i$  is the position of the frequency bin and  $r_i$  is the signal-plus-noise value, and where the shorthand notation for the summation is defined over the  $N$  frequency bins as

$$\sum_i = \sum_{i=-(N-1)/2}^{(N-1)/2}.$$

We can rewrite and then approximate the centroid estimate by

$$\begin{aligned} c &= \frac{\sum_i x_i r_i}{\sum_i \bar{r}_i + \sum_i (r_i - \bar{r}_i)} \\ &= \frac{\sum_i x_i r_i}{\sum_i \bar{r}_i \left[ 1 + \frac{\sum_i (r_i - \bar{r}_i)}{\sum_i \bar{r}_i} \right]} \\ &\approx \frac{\sum_i x_i r_i}{\sum_i \bar{r}_i} \left[ 1 - \frac{\sum_i (r_i - \bar{r}_i)}{\sum_i \bar{r}_i} + \dots \right], \end{aligned}$$

where the overbar indicates average, or expected, value. We make this expression linear by assuming that the expected value of the second term of the series expansion above is small, or

$$\left\langle \frac{\sum_i (r_i - \bar{r}_i)}{\sum_i \bar{r}_i} \right\rangle \ll 1.$$

The centroid estimate is approximated by

$$c \approx \hat{c} = \frac{\sum_i x_i r_i}{\sum_i \bar{r}_i}.$$

Thus

$$\hat{c}^2 = \frac{\sum_i \sum_j x_i x_j r_i r_j}{\left( \sum_i \bar{r}_i \right)^2}$$

and

$$\sigma_c^2 = \frac{\sum_i x_i^2 \sigma_i^2}{\left( \sum_i \bar{r}_i \right)^2},$$

where the centroid mean is assumed to be zero and where  $\sigma_i^2$  is the variance of an individual sample of the signal spectrum. The signal-plus-noise sample  $r_i$  is a magnitude-squared value.

We assume that there are  $N$  frequency bins that contain signal plus noise. We have

$$N = \frac{B_s}{B_c}, \quad (\text{A})$$

where the coherence-time bandwidth  $B_c$  is  $1/T_c$  and the bin position  $x_i = iB_c$ , and where  $B_s$  is the speckle bandwidth of the signal. The quantity  $T_c$  is the coherence time, or duration, of the first short-time FFT. We further assume that there are  $M$  noise-only pixels with  $k$  pixels on one side and  $M - k$  pixels on the other side of the  $N$  signal-plus-noise pixels. The centroid variance becomes

$$\sigma_c^2 = \frac{B_c^2 [S_k + (\sigma^2 + 1)^2 S_N + S_{M-k}]}{[M + N(\sigma^2 + 1)]^2},$$

where

$$S_N = \sum_i i^2 = \frac{N(N+1)(N-1)}{12},$$

$$S_k = k \left[ \frac{(N-1)^2}{4} + \frac{(N-1)(k+1)}{2} + \frac{(k+1)(2k+1)}{6} \right],$$

and

$$S_{M-k} = (M-k) \left[ \frac{(N-1)^2}{4} + \frac{(N-1)(M-k+1)}{2} + \frac{(M-k+1)(2M-2k+1)}{6} \right].$$

Let us make the simplifying assumption that there are no noise-only pixels; i.e., the IF bandwidth is equal to the speckle bandwidth or the centroid window just encompasses the signal spectrum. Note that this condition would apply with ideal thresholding of the output of the first short-time FFT. With this assumption both  $M$  and  $k$  are zero, and the variance of the centroid estimate becomes

$$\sigma_{\hat{c}}^2 = \frac{B_c^2(N-1)(N+1)}{12N}.$$

By using Equation A the above variance becomes

$$\sigma_{\hat{c}}^2 = \frac{B_c(B_s^2 - B_c^2)}{12B_s}.$$

If the signal and noise are Rayleigh-distributed random variables and if we assume a  $q$  spectra average before centroiding, then the simplified centroid variance becomes

$$\sigma_{\hat{c}}^2 = \frac{B_c(B_s^2 - B_c^2)}{12qB_s}.$$



**ALAN L. KACHELMYER** is a staff member in the Radar Systems group. He received a B.S. degree from the University of Minnesota, an M.S. degree from Syracuse University, and a Ph.D. from the University of Minnesota, all in electrical engineering. He has worked for the General Electric Company, Heavy Military Electronics Division, as well as for Sperry Univac, in the area of radar systems. In 1979 he joined Lincoln Laboratory and worked on the design of spread-spectrum communication systems with an emphasis on data modulation, spreading modulation, security, and error-correction coding schemes. He has also been involved in the development of microwave radar and laser radar systems with research work in various areas, including waveform design, signal processing, detection and estimation theory, passive and active tracking, and image processing. Currently he is working on problems in air defense.



**KENNETH I. SCHULTZ** is a staff member in the Systems and Analysis group. He received an S.B. degree from MIT, and M.S. and Ph.D. degrees from the University of Pennsylvania, all in electrical engineering. In 1987 he joined the Laser Radar Measurement group, where he worked on signal processing and imaging techniques for the wideband CO<sub>2</sub> range-Doppler laser radar. He has also worked on imaging and target detection techniques for passive optical imaging sensors, and he has developed laser-based imaging techniques that have medical diagnostic applications. He is currently working on a variety of problems related to air defense. From 1991 to 1993 he was chairman of the laser radar/lidar session at the International Conference on Lasers and Applications. He received the 1992 NRL Review award and the 1993 NRL Berman award for publications on satellite vibration experiments.